# Observing Tropical Cyclone Morphology Using *RADARSAT-2* and Sentinel-1 Synthetic Aperture Radar Images

JESSIE C. MOORE TORRES,[a,b] CHRISTOPHER R. JACKSON,[b,c] TYLER W. RUFF,[a,b] SEAN R. HELFRICH,[b] AND ROLAND ROMEISER[d]

[a] *Global Science and Technology, Inc., Greenbelt, Maryland*
[b] *NOAA/NESDIS/Center for Satellite Applications and Research, College Park, Maryland*
[c] *Global Ocean Associates, Alexandria, Virginia*
[d] *Rosenstiel School of Marine and Atmospheric Science, University of Miami, Miami, Florida*

(Manuscript received 23 May 2022, in final form 27 March 2023, accepted 13 April 2023)

ABSTRACT: Since the 1960s, meteorological satellites have been able to monitor tropical cyclones and typhoons. Their images have been acquired by passive remote sensing instruments that operate in the visible and infrared bands, where they only display the cloud-top structure of tropical cyclones and make it a challenge to study the air–sea interaction near the sea surface. On the other hand, active remote sensors, such as spaceborne microwave scatterometers and synthetic aperture radars (SARs), can "see" through clouds and facilitate observations of the air–sea interaction processes. However, SAR acquires images and provides the wind field at a much higher resolution, where the eye of a tropical cyclone at surface level can be identified. The backscattered signals received by the SAR can be processed into a high-resolution image and calibrated to represent the normalized radar cross section (NRCS) of the sea surface. In this study, 33 *RADARSAT-2* and 102 Sentinel-1 SAR images of Atlantic and Indian Ocean tropical cyclones and Pacific typhoons from 2016 to 2021, which display eye structure, have been statistically analyzed with ancillary tropical cyclone intensity information. To measure the size of the eye, a 34-kt ($\sim$17 m s$^{-1}$) contour is defined around it and the amount and size of pixels within the eye is utilized to provide its area in square kilometers. Additionally, an azimuthal wavenumber for each shape of the eye was assigned. Results showed that eye areas increase with decreasing wind speed and increasing wavenumber and demonstrate that SAR-derived data are useful for studying tropical cyclones at the air–sea interface and provide results of these behaviors closely to data derived from best track archives.

KEYWORDS: Oceanic waves; Tropical cyclones; Remote sensing; Satellite observations; Air-sea interaction

## 1. Introduction

Scientists started using polar-orbiting and geostationary meteorological satellite images for tropical cyclone research in the 1960s. Passive remote sensors on these satellites operate in visible and infrared bands, and only capture images of cloud-top structure, haze, or fog and not of the surface below such aerosols. Additionally, these remote sensors depend on reflected sunlight or emitted energy from clouds and Earth's surface as a radiation source and provide relatively low spatial resolution observations. Spaceborne microwave remote sensors are used to make measurements of the air–sea interface and observe through clouds (National Aeronautics and Space Administration 2020). Microwave data and imagery from the Special Sensor Microwave Imager (SSM/I) and the Tropical Rainfall Measuring Mission (TRMM) are used for such purposes, in addition to scatterometer data from the Quick Scatterometer (QuikSCAT) and Advanced Scatterometer (ASCAT). These satellite sensors can provide measurements with a spatial resolution of a few tens of kilometers. The use of spaceborne synthetic aperture radar (SAR) can observe the air–sea interface through clouds and provide higher resolution (from less than 1 to 100 m) measurements than passive microwave imagers and scatterometers do, thus resolving the constraints of other sensor types.

Tropical cyclones have been studied using SAR images since the launch of *Seasat* in June 1978, which carried the first civilian spaceborne SAR (Fu and Holt 1982). SAR does not depend on sunlight and can observe through clouds because it is an active microwave radar that emits and receives pulses at centimeter wavelengths. Additionally, radar pulses can be emitted and received at different polarizations, where the electromagnetic waves are transmitted along a plane in a specific orientation (Boerner et al. 1992). In the case of *RADARSAT-2* and Sentinel-1 SARs, signals are transmitted and received by these sensors in either vertical (V) or horizontal (H) polarization. Copolarized signals are usually strong and have specular, surface, or volume scattering, and cross-polarized signals are generally weaker and are associated with multiple scattering. However, C-band cross-polarized imagery is preferable when observing tropical cyclone imagery and its features because the ocean backscatter in this imagery has a weaker sensitivity to wind direction and incidence angle (Sapp et al. 2016).

The received backscatter power is usually calibrated to represent the sensor-independent normalized radar cross section (NRCS), which is related to surface roughness. However, the NRCS is affected by the direction and speed of sea surface winds, rain, and waves, and it depends on the radar frequency, polarization, and incidence angle. These atmospheric and oceanic processes affect the surface roughness, and with it the short Bragg waves which give rise to resonant backscattering of

*Corresponding author*: Jessie C. Moore Torres, jessie.moore.torres@noaa.gov

DOI: 10.1175/JTECH-D-22-0053.1

TABLE 1. Azimuthal wavenumbers assigned to specific eye shapes for tropical cyclone eye classification.

| Eye shape | Wavenumber |
|---|---|
| Circular | 0 |
| Circular (asymmetric) | 1 |
| Elliptical | 2 |
| Triangular | 3 |
| Square or Rectangular | 4 |
| Pentagonal | 5 |
| Hexagonal | 6 |

the microwaves (Valenzuela 1978). The NRCS is proportional to the intensity of the Bragg waves; therefore, it increases with wind speed. A mirrorlike surface does not provide a backscattered signal and leaves dark patterns in SAR images. For a given wind speed, the NRCS has the largest values when the radar is looking into or against the wind direction and minima in the two look directions perpendicular to the wind. The incidence angle plays a role in Bragg scattering theory, where it depends on the surface waves to match the radar wavelength projected onto that same surface, therefore classifying them as "Bragg waves" (Valenzuela 1978; Monaldo and Beal 2004). The majority of C-band SARs at incidence angles in between 20° and 60° utilize the following expression of NRCS in the following form (or parameterizations of this form, along with various combinations of coefficients):

$$\sigma_0 = A(U_{10}, \theta)[1 + b_1(U_{10},\theta)\cos\phi + b_2(U_{10},\theta)\cos 2\phi]^B. \quad (1)$$

The NRCS value is represented as $\sigma_0$, in addition to variables such as the wind speed at 10 m height ($U_{10}$), the incidence angle ($\theta$), the angle between the radar look direction and the local wind direction ($\phi$), and constants that depend on the radar frequency, polarization, $\theta$, and $U_{10}$. Thus, it is important to know the NRCS values of a SAR image as they provide information on the air–sea interaction occurring in the presence of a tropical cyclone.

Compared to the first civilian spaceborne microwave SAR on board *Seasat*, the SARs of *RADARSAT-1* and *Envisat* had more polarization options and better spatial resolution and coverage. Previously, Li et al. (2013) used *RADARSAT-1* and *Envisat* SAR images of tropical cyclones to generate SAR-derived statistics on the ocean surface response to tropical cyclones. Additionally, *RADARSAT-1* SAR hurricane imagery was utilized in characterizing the ocean surface response to tropical cyclone wind and rain (Friedman and Li 2000), discovering roll vortices associated with the rainbands of a hurricane (Katsaros et al. 2000), and detailing refraction of hurricane-generated oceanic swell waves (Li et al. 2002), among others. Likewise, authors like Reppucci et al. (2010) utilized *Envisat* SAR hurricane images to develop and validate a tropical cyclone intensity retrieval method. However, because these satellites are no longer operating, more recent SAR imagery from *RADARSAT-2* and the Sentinel-1 mission were used for this examination.

*RADARSAT-2* was launched by the Canadian Space Agency (CSA) on 14 December 2007 and is operated by MacDonald, Dettwiler, and Associates (MDA). It is the follow-on satellite of *RADARSAT-1*. *RADARSAT-2* has a C-band SAR with fully polarimetric (HH, HV, VH, VV) imaging capability. In this study, we used ScanSAR wide (SCW) mode images. ScanSAR uses two or more single beams to cover adjoining gaps in an alternating manner and it provides a much wider swath, up to 500 km, than the other modes (Maxar Technologies 2018). The resolution (range and azimuth) is 168–73 m × 78–106 m (European Space Agency 2022).

Sentinel-1 is an imaging radar mission comprised of two polar-orbiting satellites launched by the European Space Agency (ESA). The Sentinel-1 mission includes a C-band SAR

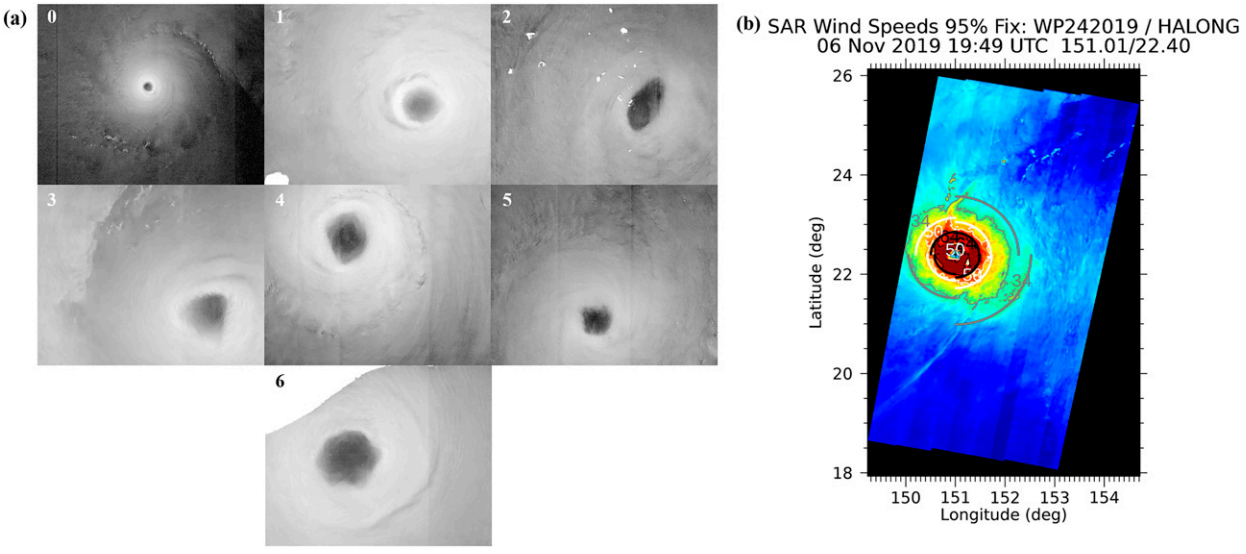


FIG. 1. (a) Examples of SAR hurricane and typhoon imagery and (b) an example of a contour map for Typhoon Halong at 1949:06 UTC 6 Nov 2019 (Center for Satellite Applications and Research 2020).

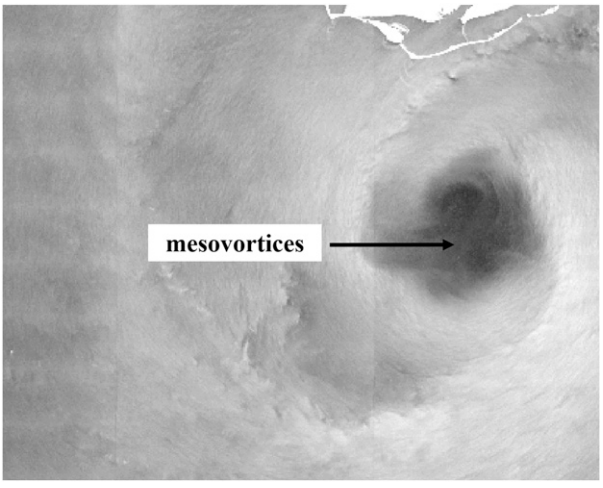


FIG. 2. SAR NRCS image from *Sentinel-1A* (VH polarization) of hurricane Hermine showing an example of a mesovortex at 0123:45 UTC 1 Sep 2016 in the Gulf of Mexico (Center for Satellite Applications and Research 2020).

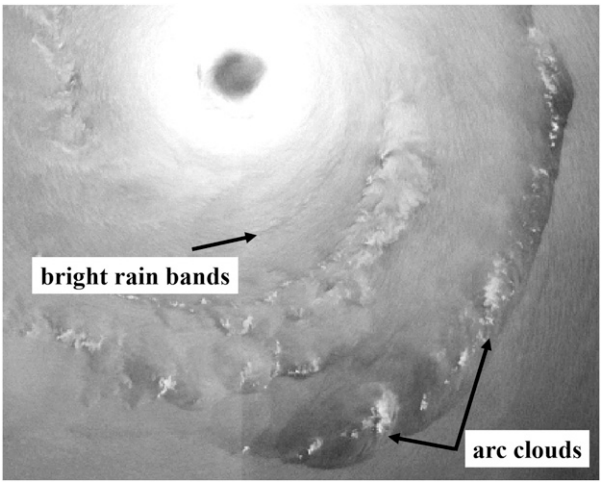


FIG. 3. SAR NRCS image from *Sentinel-1A* (VH polarization) of hurricane Dorian at 2246:52 UTC 30 Aug 2019 showing examples of arc clouds and rainbands (Center for Satellite Applications and Research 2020).

instrument that acquires data in four modes: 1) strip map (SM), 2) interferometric wide swath (IW), 3) extra wide swath (EW), and 4) wave (WV) modes. The Sentinel-1 imagery used in this study were mostly acquired in IW and EW modes. The IW mode acquires data with a 250 km swath at a single look 5 m $\times$ 20 m spatial resolution and the EW mode acquires data over a 400 km swath at a 20 m $\times$ 40 m spatial resolution. Both of these modes employ a technique called the terrain observation with progressive scans SAR (TOPSAR) technique, which captures the SAR data in subswaths. The IW mode captures three subswaths, whereas the EW mode captures five subswaths (European Space Agency 2020).

As previously mentioned, the NRCS of a SAR image can provide information on a tropical cyclone's air–sea interaction. However, not many case studies using SAR-derived information for tropical cyclone research provide detailed information on the sea surface response from tropical cyclone wind forcing. Additionally, SAR images can be inconsistent when classifying and segmenting images and can be affected depending on the conditions used for their physical retrieval and the amount of speckle noise present in the imagery. Therefore, it is important not to generalize tropical cyclone case studies (Li et al. 2013). The SAR copolarized NRCS may saturate under high wind speed conditions making some geophysical model functions (GMF) no longer

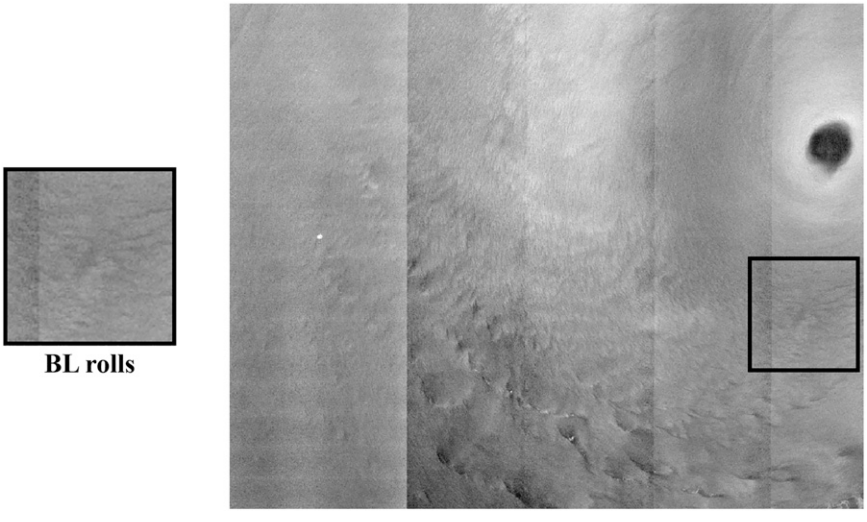


FIG. 4. (right) SAR NRCS image from *Sentinel-1A* (VH polarization) of Typhoon Shanshan located south of Japan at 0832:38 UTC 7 Aug 2018 and (left) a close-up within the image showing its BL rolls (Center for Satellite Applications and Research 2020).

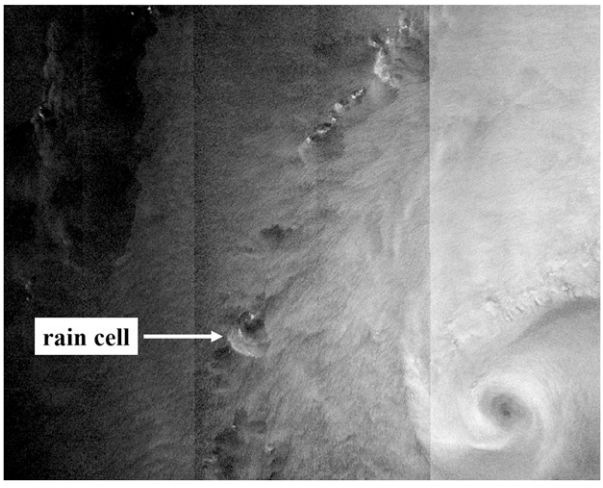


FIG. 5. SAR NRCS image from *Sentinel-1A* (VH polarization) of tropical storm Florence at 0939:40 UTC 8 Sep 2018 in the Atlantic Ocean. Rain cells are forming to the west of the eye (Center for Satellite Applications and Research 2020).

valid for 10 m wind retrievals above the sea surface (Zhang and Perrie 2014).

The purpose of this study was to generate SAR-derived cyclone statistics to determine a relationship between the area and shape of the eye of a tropical cyclone and its intensity based on the NRCS of tropical cyclones in SAR images. In addition, we have identified other fine-scale structures within a tropical cyclone, such as mesovortices, arc clouds, and double eyewalls using 33 *RADARSAT-2* and 102 Sentinel-1 SAR images of tropical cyclone eye "hits" from the Atlantic, Indian, and Pacific Oceans. Eye hits are defined as SAR imagery that include the eye of a tropical cyclone.

## 2. Methods

### *a.* RADARSAT-2 *and Sentinel-1 imagery*

The study areas of the Atlantic, Indian, and Pacific Oceans are based on the availability of SAR tropical cyclone eye imagery on the National Oceanic and Atmospheric Administration's (NOAA) Center for Satellite Applications and Research (STAR) Tropical Storm Cyclone Winds page (https://www.star.nesdis.noaa.gov/socd/mecb/sar/AKDEMO_products/APL_winds/tropical/index.html). NOAA provides the SAR NRCS and wind images and data in Network Common Data Form (netCDF) format in 500 m spatial resolution. The storms that were included in this project were from 2016 until 2021. Additionally, all Sentinel-1 and *RADARSAT-2* SAR imagery has been acquired at a cross polarization of VH (vertical transmit, horizontal receive).

Utilizing SAR imagery, we were able to identify a variety of oceanic and atmospheric features that are typically present in the air–sea interface, such as mesovortices, rainbands and arc clouds, boundary layer (BL) rolls, and rain cells. Additionally, we are able to identify features such as double eyewalls, which are features that are also important to see in the imagery, given that they indicate that a storm is undergoing the eyewall replacement cycle (ERC). It is equally important to study trends in storm intensity and morphology as it is to have the ability to identify these features in the imagery, as they can contribute to our understanding of their role in tropical cyclone formation. The following methods that were used to achieve this are mostly based on the Li et al. (2013) study on tropical cyclone eye morphology with SAR imagery.

### *b. Storm intensity data*

Storm intensity data are obtained from the North Atlantic Hurricane Database (HURDAT) best track data for hurricanes. Best track data for typhoons are obtained from the Japan Meteorological Agency Regional Specialized Meteorological Center (RSMC) and the Joint Typhoon Warning Center (JTWC), and data from Indian Ocean tropical cyclones are from the National Center for Atmospheric Research (NCAR) International Best Track Archive for Climate Stewardship (IBTrACS). All datasets provide intensity data (maximum 1-min surface winds speed in knots and minimum central pressures in hPa) every 6 h throughout each track and its center locations. After this information was obtained, along with the NRCS images, a spreadsheet was created. This file has a list containing information of each SAR NRCS image, such as storm name, intensity, and parameters for radial winds. Parameters for radial winds for all quadrants of each SAR image can also be found in the NOAA STAR Tropical Cyclone Winds page. Additionally, eye hits of storms that were less than a category 1 in the best track data were excluded from the study.

### *c. Tropical cyclone eye classification and measurements*

Before measuring the size of the eye in each tropical cyclone image, the shape of each eye was classified individually in order to determine if its morphology is related to intensity. This was done by visually assigning an azimuthal "wavenumber" to each SAR image based on specific eye characteristics described in Li et al. (2013), where the wavenumber values are assigned based on the eye's resemblance to specific shapes (Table 1; Fig. 1a). Azimuthal wavenumbers describe the asymmetry of the hurricane eye with the length of the radius from the eye center coordinates as a function of the degree along the eye contour (Vinour et al. 2021).

Once a wavenumber was assigned to each eye shape (Fig. 1a), the size of the eye was quantified. Eye area is vital to know as well as the eye shape, given that numerous studies have tried to understand the thermodynamics involved when observing how the eyewall and tropical cyclone circulation contribute to eye morphology (Smith 1980; Shapiro and Willoughby 1982; Willoughby 1990). Additionally, it has been observed that the eye typically contracts during intensification. In a SAR NRCS image of a tropical cyclone, areas with high winds and rain show as bright around the eye, whereas the NRCS is dark within the eye because of the lower wind. Based on this concept, eye areas for this study were calculated by identifying a 34-kt (1 kt $\approx$ 0.51 m $s^{-1}$)

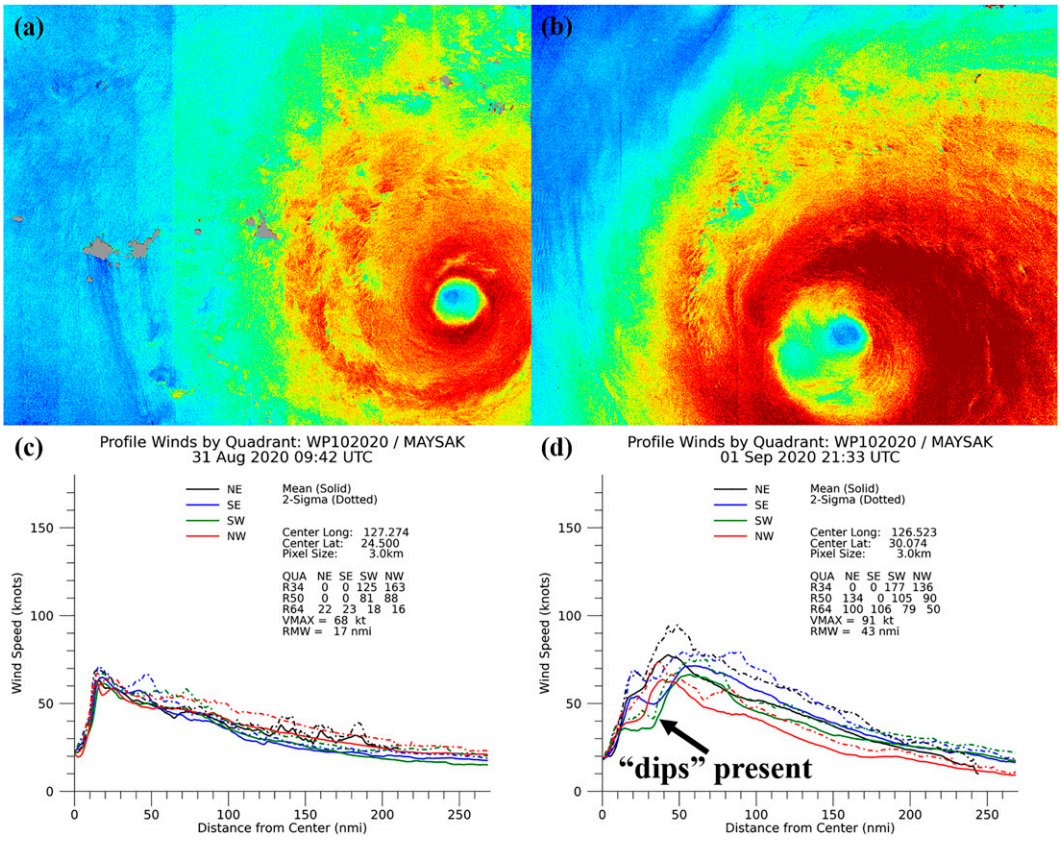


FIG. 6. (a) SAR wind speed images from *RADARSAT-2* (VH polarization) of Typhoon Maysak with a double eyewall present, (b) another *RADARSAT-2* SAR-derived wind speed image of Maysak, (c) SAR-derived wind plot at 0942 UTC 31 Aug 2020, and (d) wind plot at 2133 UTC 1 Sep 2020 (Center for Satellite Applications and Research 2020).

wind speed contour around the eye (Fig. 1b) and utilizing amount and size of pixels within the eye to provide the eye area in square kilometers. Size and area of pixels varied by imagery source and both are taken into account when making these calculations. This was calculated for tropical cyclone imagery with eyes that are completely visible in SAR imagery (therefore, SAR images with partial eye hits were excluded from this study). This information was added to the spreadsheet with all other SAR-derived and best track parameters. SAR-derived parameters obtained from NOAA STAR Tropical Cyclone Winds page, like wind speed, were calculated by using a C-band GMF algorithm (Hersbach et al. 2007), which relates the NRCS of the ocean surface to wind based on the Bragg scattering theory. The radius of maximum winds, another parameter observed in this study, is a value calculated by extracting the distance between a storm's eye center and the band that contains the maximum wind speed.

### *d. Observing atmospheric and oceanic features with SAR imagery*

#### 1) MESOVORTICES

Vortical features within the eyewall are apparent when observing visible imagery of hurricanes. These intense vorticity features within the eyewall of tropical cyclones are known as mesovortices, and can be identified in SAR imagery when low-level circulations bordering the eyewall are apparent. Montgomery et al. (2002) studied this feature with an experimental apparatus to emulate the fluid dynamics of the tropospheric flow in the eyewall. They suggested that they are formed from instability within the eye of a storm along with vorticity in the eyewall and contribute to hurricane intensification. Additionally, eye–eyewall mesovortices may be responsible for transferring high entropy air from the low-level eye to the eyewall (Montgomery et al. 2006). The use of SAR to observe these features provides evidence (Fig. 2) that they exist in lower levels of a tropical cyclone, rather than just the upper levels (Li et al. 2013; Zhang and Li 2017).

#### 2) RAINBANDS AND ARC CLOUDS

Beyond the impact of mesovortices, it is also important to study the rainbands and arc clouds of a tropical cyclone. Visually, the SAR NRCS images were examined in order to identify rainband and arc clouds features, which would typically be seen as three different types of signatures: dark, bright, or dark and bright rainbands (Fig. 3). Changes in sea surface roughness are caused by a variety of tropical cyclone mechanisms (i.e., rain and wind gusts), which is why there appears

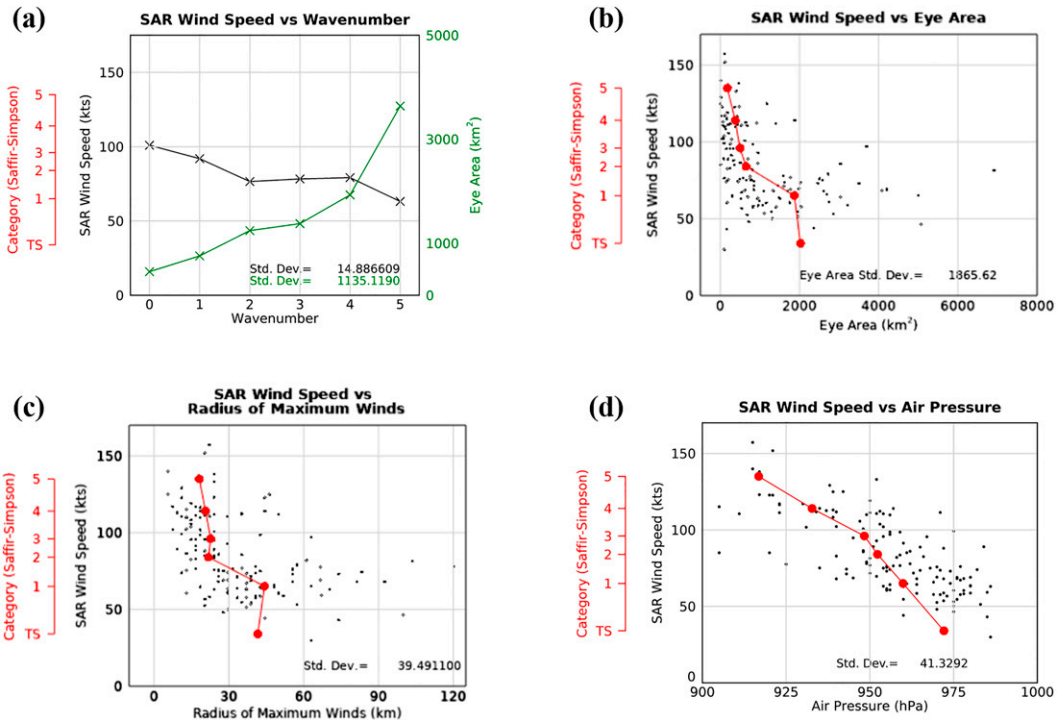


FIG. 7. Plots summarizing storm statistics with a (a) line plot showing the mean SAR wind speed (black) and eye area (green) according to wavenumber, (b) scatterplot of SAR wind speed and eye area and the mean (red) represented according to SAR wind speed and category, (c) scatterplot of SAR wind speed and radius of maximum winds and the mean (red) represented according to SAR wind speed and category, and a (d) scatterplot of SAR wind speed and air pressure (obtained from best track data) and the mean (red) represented according to SAR wind speed and category.

to be more than one signature to identify the rainbands (Bliven and Giovanangeli 1993). Rainbands produce large amounts of rainfall and cause floods during landfall (Zhang and Li 2017). Some studies have suggested that in intense storms, rainbands may evolve into a secondary eyewall, trigger an ERC, and influence storm intensity (Houze et al. 2007).

Arc clouds can be found not only in a midlatitude thunderstorm and mesoscale convective systems, but also in tropical cyclone environments, according to previous studies (Knaff and Weaver 2000). Similar to primary rainbands, arc clouds can have a length of several hundred kilometers (Zhang and Li 2017). Regarding surface scattering based on the Bragg scattering theory, raindrops produced from these arc clouds generate ring waves on the sea surface, which scatter the incident radar pulse (Alpers et al. 2016), and can therefore identify arc clouds in SAR NRCS images (Fig. 3). Arc clouds usually move away from the convective core region and can also inhibit tropical cyclone development in the short term by promoting downdrafts locally and low to midlevel outflow and bringing cool, dry air down into the boundary layer (Dunion et al. 2010).

### 3) BOUNDARY LAYER ROLLS

BL rolls, also called "roll vortices," are another feature to consider when observing tropical cyclones. BL rolls can influence the turbulent exchange of momentum, sensible heat, and moisture, which is essential to consider for tropical hurricane maintenance and intensification (Zhang et al. 2008). There are high surface wind speeds present when BL rolls are formed. This suggests that the tropical cyclone boundary layer is a favorable environment for roll formation (Foster 2005). This can cause streak patterns in sea surface roughness and be visible in SAR imagery (Zhang et al. 2008; Fig. 4). In a SAR image, they are typically found in line with wind direction when performing a fast Fourier transform (FFT) analysis on the SAR signal (Li et al. 2013) and therefore are identifiable.

### 4) RAIN CELLS

Rain cells can be observed because their signatures in the SAR NRCS images are caused by the modification of the sea surface roughness by raindrops and airflow (spreading downdraft) impacting the sea surface. Such rain cells typically have diameters of 5–10 km. The rain cell signature on these images (Fig. 5) varies, where, sometimes, they show as a somewhat circular pattern that is entirely or partially bright (depending on the strong ambient wind), or partially bright and dark. Additionally, rain cells can also appear as irregular dark and bright patches in radar signatures of spreading downdrafts (Melsheimer et al. 2001). Rainbands, in comparison to rain cells, display as elongated patterns.

### 5) DOUBLE EYEWALLS

Double eyewalls appear in SAR images when a tropical cyclone is undergoing an ERC. ERCs occur in intense tropical

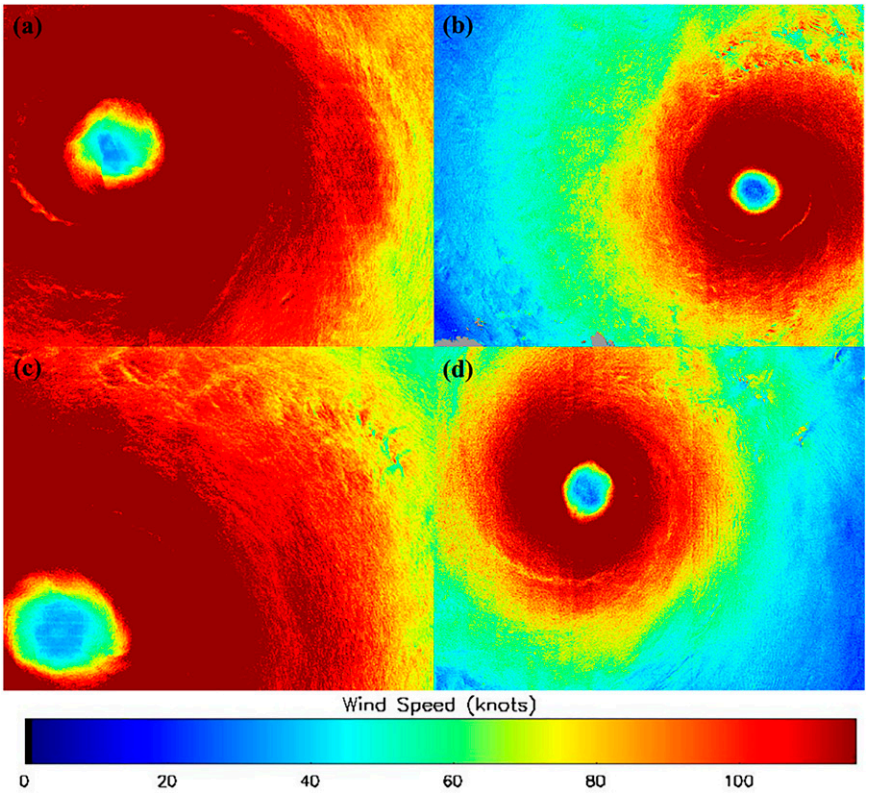


FIG. 8. SAR imagery of Surigae acquired at (a) 2122 UTC 18 Apr 2021 with a wavenumber of 1, (b) 2129 UTC 19 Apr 2021 with a wavenumber of 1, (c) 0942 UTC 20 Apr 2021 with a wavenumber of 1, and (d) 0944 UTC 21 Apr 2021 with a wavenumber of 2.

cyclones where winds are greater than 185 km $h^{-1}$ (100 kt), or at a category 3 hurricane and above. The eyewall contracts, and the rainbands strengthen to form an outer eyewall (therefore converting the original eyewall into an "inner eyewall"). The tropical cyclone temporarily weakens while the outer eyewall replaces the inner eyewall, but then it reintensifies when the outer eyewall has completely replaced the inner eyewall. Additionally, the maximum wind speed of the inner eyewall decreases during the formation of the outer eyewall (Sitkowski et al. 2011; Zhang and Perrie 2018).

In addition to observation of the NRCS SAR images, we depended on the SAR mean winds from NOAA STAR's Tropical Cyclone Winds page to confirm the presence of a double eyewall in the images. Additionally, these radial wind profiles provide the quadrants in which the double eyewall falls into each tropical cyclone. For Typhoon Maysak, we were able to obtain more than one eye hit and compare the images of the storm from when it was a category 1 storm (best track) at 0942 UTC 31 August 2020 (Fig. 6a) and when it had strengthened to by 10 kt at 2133 UTC 1 September 2020 (Fig. 6b). While one could see the double eyewall's presence in Fig. 6b, the SAR wind plot in Fig. 6d confirms its presence by showing "dips" in most quadrants of the tropical cyclone. For comparison, when Maysak was weaker the previous day (Fig. 6a), the double eyewall was not present and the SAR wind plot for that image (Fig. 6c) confirms the absence of the double eyewall because of its lack of "dips." However, because strong, concentrated rainbands around the area of maximum winds can attenuate the radar signal, the wind speeds derived in these regions may be reduced (Vinour et al. 2021). This is a factor to consider when determining the presence of a double eyewall in a SAR image.

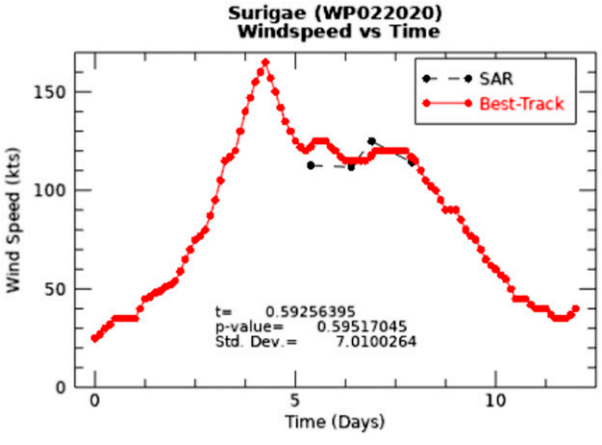


FIG. 9. Plot showing Surigae SAR wind speed and time of data acquisition according to the best track (red) data and SAR data (black). The plot also shows *p* value, standard deviation, and *t* value.

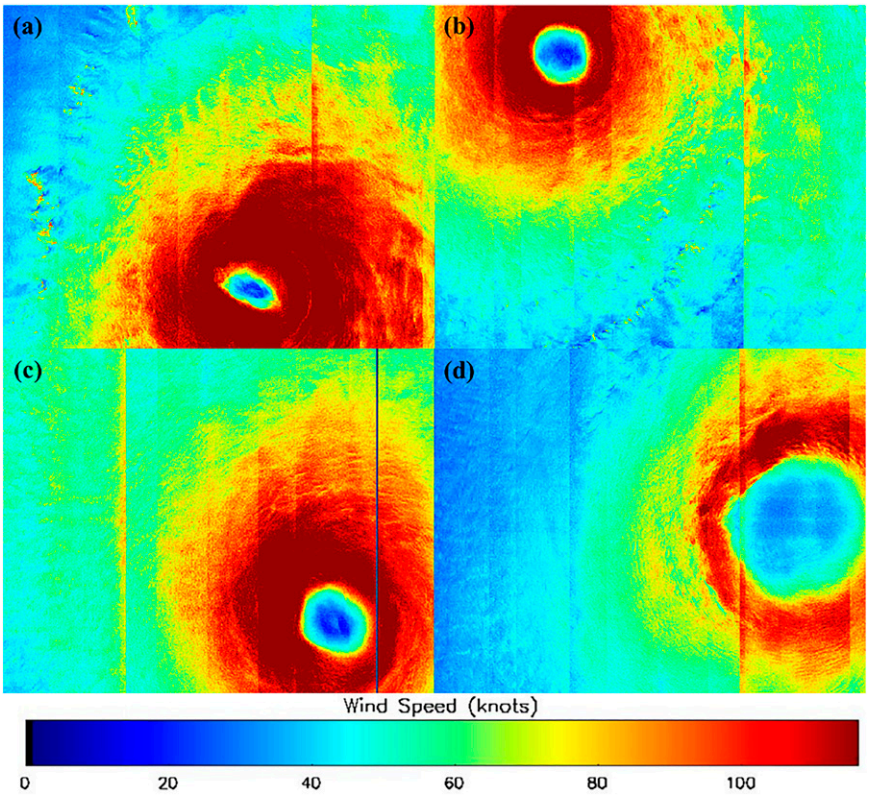


FIG. 10. SAR imagery of Sergio acquired at (a) 1341 UTC 3 Oct 2018 with a wavenumber of 2, (b) 1406 UTC 6 Oct 2018 with a wavenumber of 0, (c) 0234 UTC 7 Oct 2018 with a wavenumber of 4, and (d) 0944 UTC 9 Oct 2018 with a wavenumber of 4.

## 3. Results

### a. *Overall statistics*

After collecting SAR NRCS images of tropical cyclone eye hits from 2016 to 2021 and having their information compiled in a spreadsheet, we carried out a variety of statistical analyses to find a relationship among variables such as eye area, shape, pressure, radius of maximum winds and SAR-derived storm intensity. Additionally, storms were also observed individually if they had three or more eye hits.

In this study, a total of 135 SAR images were utilized. Seven outliers for the calculated eye areas were excluded after applying the interquartile range method (IQR). To compare the data, we observed a relationship between the SAR-derived and best track parameters (Fig. 7). Figure 7a shows that decreasing wind speeds and increasing eye areas were present in higher wavenumbers. At wavenumbers 4 and 5, both eye area and wind speed drastically increased and decreased, and at wavenumber 4, although not significant, there is a slight increase in the SAR wind speed, suggesting that there may be some factors affecting this, such as the strengthening of the eyewall and near-core wind gradients that cause the contraction of high-wind areas (Vinour et al. 2021). In Fig. 7b, one can observe that eye areas increase while wind speeds decrease. In this case, on average, eye areas in category 1–2 storms increased ~1218 km$^2$ while wind speed decreased ~20 kt. In comparison, eye areas in category 2–5 storms increased ~475 km$^2$ while wind speed decreased ~35 kt between them. These numbers display the presence of a smaller increase in eye area with larger decreases in wind speeds (categories 2–5) while there is a larger increase in eye areas with smaller decreases in wind speeds (categories 1–2). Figure 7c supports this observation, where the radius of maximum winds increases with

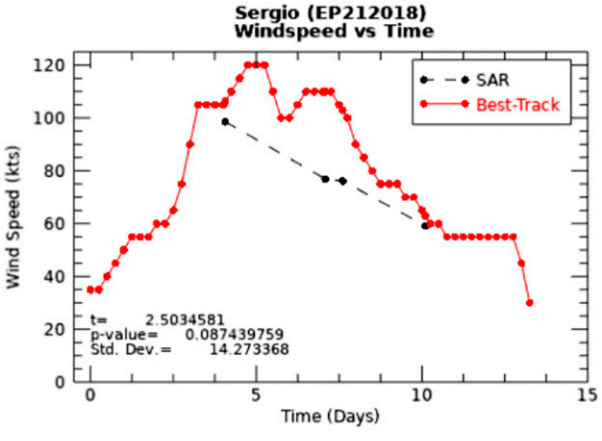


FIG. 11. Plot showing Sergio SAR wind speed and time of data acquisition according to the best track (red) data and SAR data (black). The plot also shows *p* value, standard deviation, and *t* value.

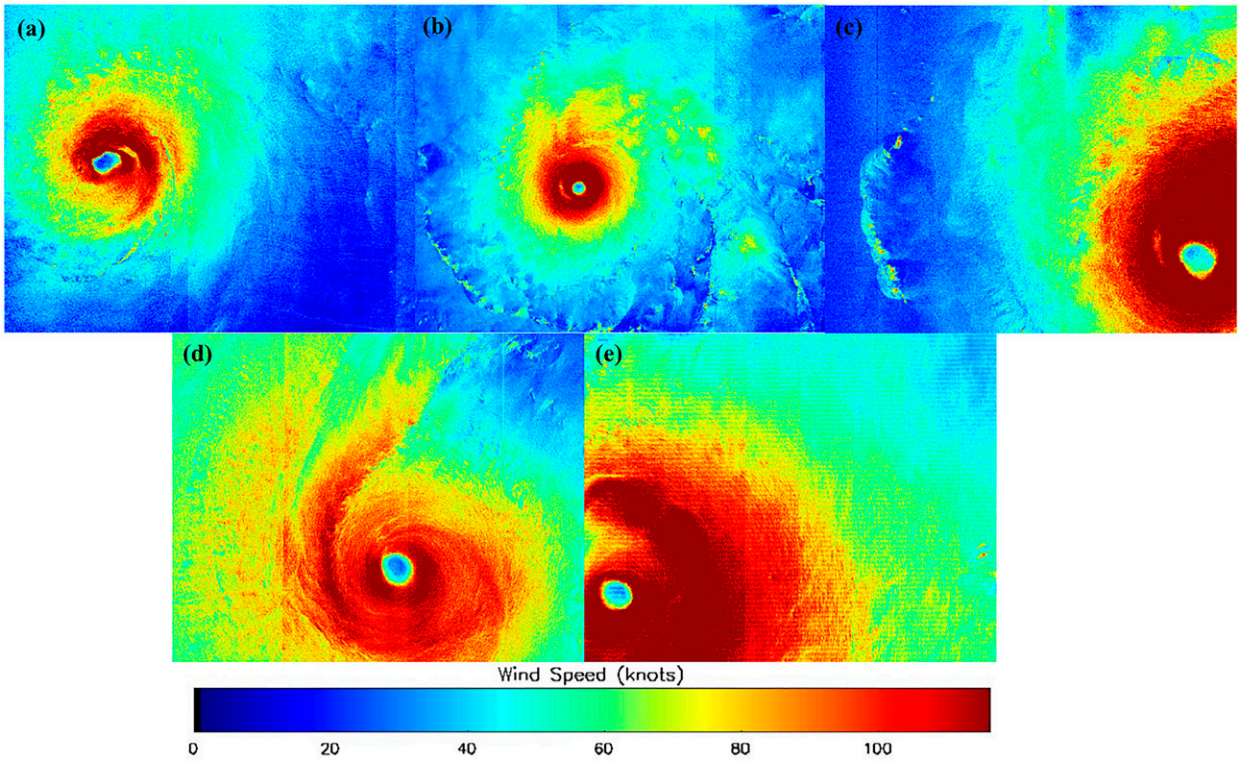


FIG. 12. SAR imagery of Sam acquired at (a) 2104 UTC 24 Sep 2021 with a wavenumber of 4, (b) 0910 UTC 26 Sep 2021 with a wavenumber of 0, (c) 0958 UTC 30 Sep 2021 with a wavenumber of 3, (d) 2151 UTC 2 Oct 2021 with a wavenumber of 1, and (e) 2122 UTC 3 Oct 2021 with a wavenumber of 1.

decreasing speed. On average, there was a drastic increase in radius of maximum winds by a difference of ~20 km while there was a decrease in wind speed by a difference of ~30 kt between category 2 and category 1 storms. Additionally, there was an increase of ~2 km from category 5 to category 2 storms while there was a decrease of ~70 kt between them. Figure 7d shows air pressure increasing with decreasing wind speed; however, its behavior involves a constant decrease in SAR wind speed with increasing air pressure, which is a behavior that is commonly seen in best track data.

### *b. Storm-specific statistics*

#### 1) SURIGAE

Surigae had four eye hits acquired (Fig. 8). This provides an opportunity to study changes in wind speed over time among the SAR imagery and compare these changes to best track wind speed over time (Fig. 9). Paired Student's $t$ tests and $p$ values were calculated with the SAR-derived wind speed versus best track wind speed using Interactive Data Language (IDL) software for each figure. For Surigae, the $t$ value and $p$ value indicate that there is no statistical significance between the SAR-derived wind speed and the best track wind speed, meaning that there is not much difference between both measurements. It is important to note the amount of points present between the SAR measurements and the best track measurements, given that SAR acquisitions are limited.

#### 2) SERGIO

Sergio had four eye hits acquired through SAR (Figs. 10 and 11). This storm's results indicate that there may be a meaningful difference between the SAR-derived wind speed and the best track wind speed, but the difference is not strong

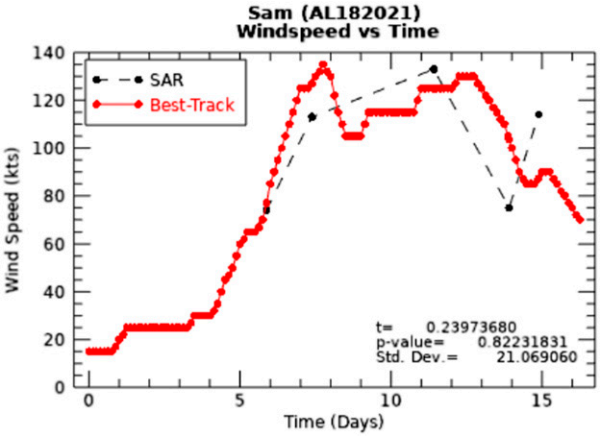


FIG. 13. Plot showing Sam SAR wind speed and time of data acquisition according to the best track (red) data and SAR data (black). The plot also shows $p$ value, standard deviation, and $t$ value.

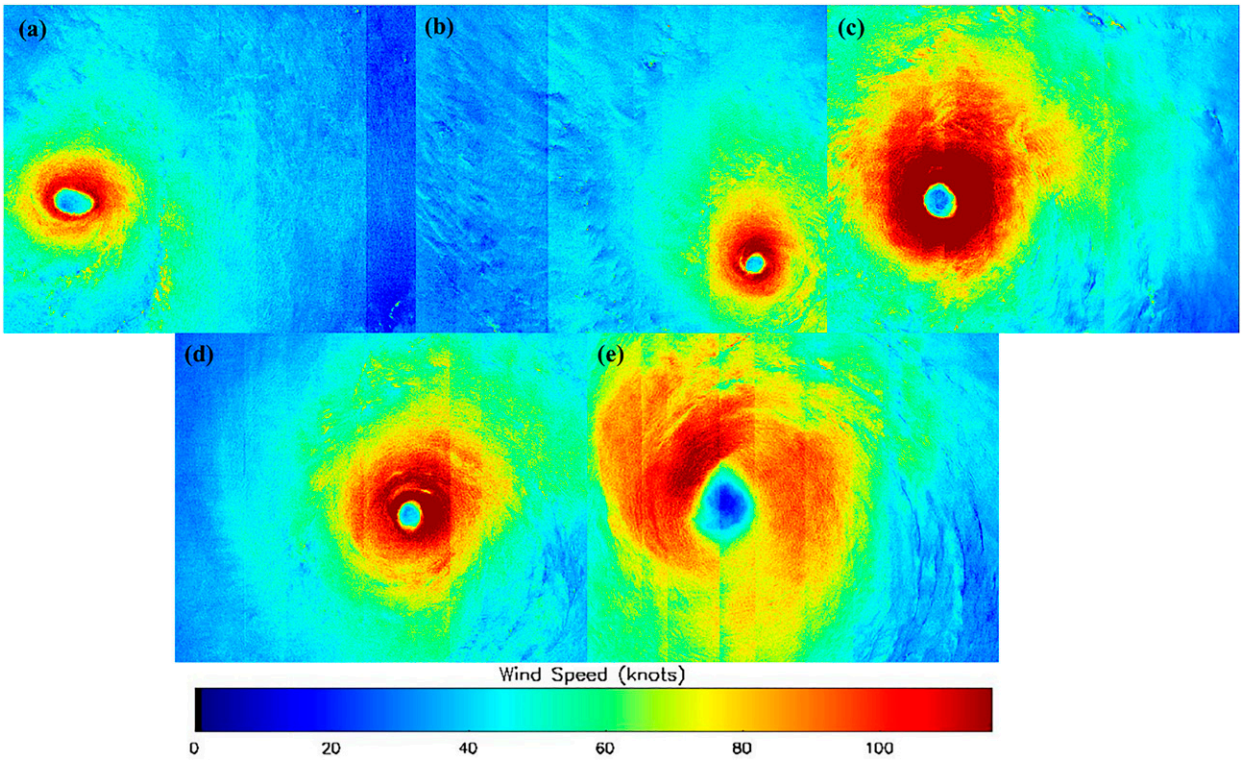


FIG. 14. SAR imagery of Marie acquired at (a) 1339 UTC 1 Oct 2020 with a wavenumber of 2, (b) 0223 UTC 2 Oct 2020 with a wavenumber of 5, (c) 0227 UTC 3 Oct 2020 with a wavenumber of 1, (d) 1420 UTC 3 Oct 2020 with a wavenumber of 1, and (e) 1429 UTC 4 Oct 2020 with a wavenumber of 4.

enough to indicate statistical significance. The SAR wind speeds show an almost constant decrease over time, while the best track measurements show brief moments on increase and decrease in wind speed over time. The difference in trendline behaviors are due to the lack of SAR acquisitions during peak wind speeds. Wavenumbers in the SAR imagery increase in the last two acquisitions while the overall trend of the SAR wind speeds decrease.

### 3) SAM

Sam's five eye hits can be seen (Figs. 12 and 13) following a trend that briefly follows the best track wind speed. A difference between both sources of wind speeds is considered to be statistically insignificant. In comparison to the previous storms discussed, Sam has one additional eye hit, therefore improving the representation of the SAR data by increasing the sample size. However, day 15 of the SAR wind speed measurement, 115 kt, which is higher than the best track value of 85 kt (Fig. 13), is a result of the presence of rain attenuation closer to the northwest quadrant of the storm (Fig. 12e). Its wavenumbers do not have a particular relationship with the behavior of the SAR wind speeds.

### 4) MARIE

The SAR wind speed for Marie's acquisitions (Fig. 14) can be seen to behave in a similar trend as the SAR best track data (Fig. 15), where there is an increase in wind speed and then a decrease after it reaches its peak at just over 100 kt. Marie's wind speeds are statistically significant and the observed difference is likely to be meaningful. Marie's wavenumber at the peak is 1, while the wavenumber increases at the lower ends of the trend. However, it is not certain if this indicates a specific relationship between the behavior of this particular storm and the wavenumbers.

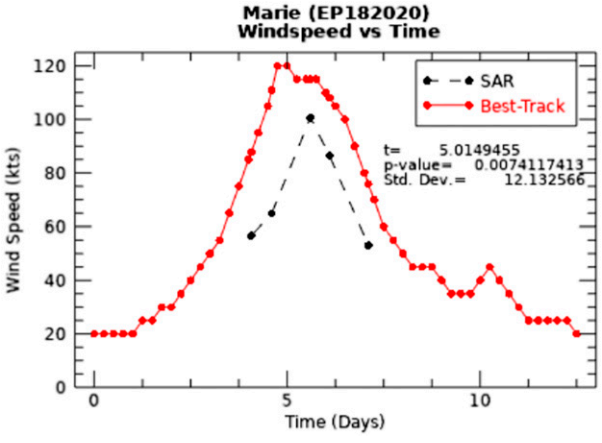


FIG. 15. Plot showing Marie SAR wind speed and time of data acquisition according to the best track (red) data and SAR data (black). The plot also shows *p* value, standard deviation, and *t* value.

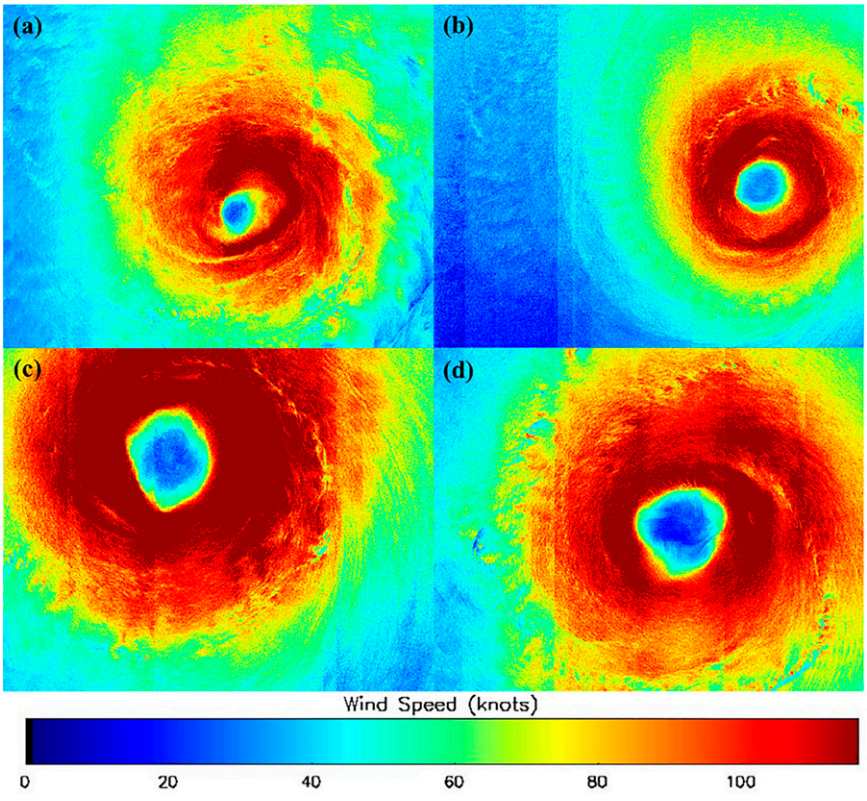


FIG. 16. SAR imagery of Larry acquired at (a) 0852 UTC 4 Sep 2021 with a wavenumber of 2, (b) 2134 UTC 5 Sep 2021 with a wavenumber of 1, (c) 0924 UTC 6 Sep 2021 with a wavenumber of 4, and (d) 0928 UTC 7 Sep 2021 with a wavenumber of 4.

#### 5) LARRY

Larry (Figs. 16 and 17) displays an unclear trend regarding the SAR wind speed, but its $p$ value proves it to be statistically significant, which indicates a high difference in the SAR and best track wind speeds, with wind speed measurements being meaningful in accordance to the $t$ value. Larry's wavenumbers do not indicate a relationship with the SAR wind speed behavior.

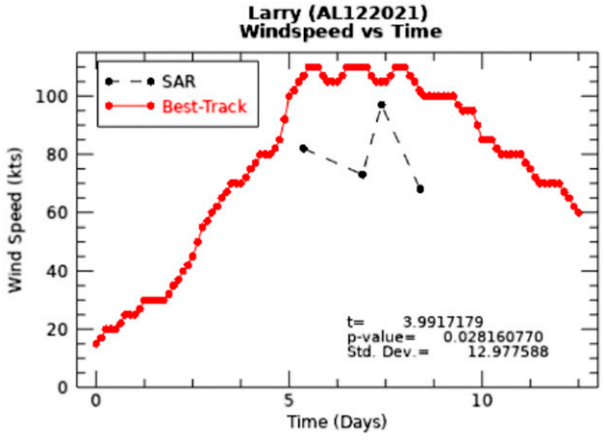


FIG. 17. Plot showing Larry SAR wind speed and time of data acquisition according to the best track (red) data and SAR data (black). The plot also shows $p$ value, standard deviation, and $t$ value.

## 4. Conclusions

The purpose of this study was to utilize 33 *RADARSAT-2* and 102 Sentinel-1 images to determine if there is a relationship between eye area, shape, and storm intensity by measuring the eye and classifying its shape and using best track data of the storms that had eye hits. SAR images allow us to observe and study ocean surface response to tropical cyclones, especially since SARs can "see" through clouds. Based on the data obtained from these images, we found that wavenumber 0 (symmetric and circular eyes) had the highest wind speed and wavenumber 5 (pentagonal) had the lowest (Fig. 7a). This fact shows us that, just like in the upper-level structure of tropical cyclones, intense storms tend to develop extremely small and circular eyes at the air–sea interface.

In this study, we were also able to compare other SAR-derived and best track parameters, such as eye area, air pressure, and the radius of maximum winds. Comparison results showed that air pressure increases with decreases in SAR wind speed (Fig. 7d). Additionally, we observed that eye area increases as wavenumber increases (therefore, it has an inverse relationship with SAR wind speed with respect to wavenumber).

Wavenumber 5 has the largest eye area while wavenumber 0 has the lowest (Fig. 7a). Eye area, when only compared to SAR wind speed (Fig. 7b), increases as the wind speed decreases (which matches the trends when compared to wavenumber as well in Fig. 7a). This trend was generally the case; however, category 2–5 storms showed a sharper decrease in wind speed than in category 1–2 storms as eye area increased. This is also true when SAR wind speed is compared to the radius of maximum winds, where an increasing radius is present at lower wind speeds (Fig. 7c). Since the radius is a component of the eye of a tropical cyclone, it explains the similar behaviors in their data.

Tropical cyclones with several eye hits were observed relative to their SAR-derived and best track wind speeds across time in order to estimate the accuracy of the SAR data for observing trends in intensity in tropical cyclones (Figs. 8 and 17). Storms such as Larry and Marie presented as statistically significant in the differences between their SAR-derived and best track wind speeds (Figs. 15 and 17). This is without considering the amount of wind acquisition estimates in the SAR data versus those from the best track data due to the limited nature of SAR data acquisition.

We were also able to observe and identify features in the SAR imagery such as mesovortices, rainbands, rain cells, double eyewalls, arc clouds, and BL rolls. Mesovortices are one of the many important features in a tropical cyclone because they contribute to hurricane intensification due to their vortical nature that transfers high entropy air from the low-level eye to the eyewall (Montgomery et al. 2006). Rainbands and arc clouds display different types of signatures due to rain attenuation affecting sea surface roughness. Arc clouds usually move away from the convective core region of a tropical cyclone and can be used to identify rain effects in SAR images. By identifying these signatures, one can estimate the amount of rainfall a storm will bring, which is pivotal when preparing for flood events. Rainbands also evolve into a secondary eyewall in a tropical cyclone, which tend to trigger an ERC and affect tropical cyclone intensity (Houze et al. 2007). This secondary eyewall, also called a double eyewall, is a result of rainbands strengthening to form the outer eyewall, causing brief intensification, followed by a brief weakening before reintensifying. Radial wind profiles (Fig. 6) can be used to determine the presence or absence of a double eyewall in a SAR image, but because of rain attenuation affecting intensity estimates from SAR, this is something that is still being studied. BL rolls influence the exchange of momentum, heat, and moisture in a tropical cyclone across its boundary layer, and can be seen as streak patterns in SAR imagery, especially since they are found in-line with wind direction (Li et al. 2013). Mesovortices were the feature that was least present among all of the SAR images analyzed in this study, while BL rolls were the most frequent. Additionally, it was noticed that 73% of rain cells, 72% of arc clouds, and 65% of BL rolls were seen in SAR images that were acquired in the tropics during their acquisition times.

In future studies, assigning wavenumbers with an algorithmic approach could be done to accurately assign these numbers to each tropical cyclone eye. By doing so, this could give forecasters and the meteorology community as a whole more and reliable information regarding how wavenumbers may or may not indicate potential increases or decreases in active tropical cyclone intensities. Additionally, implementing rain rate data into SAR tropical cyclone research can help provide better estimates in SAR wind data and therefore more accurate data for forecasters to implement in weather models.

*Acknowledgments.* This work was prepared with funding and resources from Global Science and Technology, Inc., and NOAA NESDIS Center for Satellite Applications and Research. Resources and software licenses from the University of Miami Rosenstiel School of Marine and Atmospheric Science were also utilized for a preliminary version of this paper. We thank Dr. Xiaofeng Li for assisting with the preliminary version of this paper and Dr. Samir Chettri for providing the tools and resources necessary in order to complete this project. Part of this work was performed and funded under ST13301CQ0050/1332KP22FNEED0042.

*Data availability statement.* The SAR wind estimates and imagery utilized in this study are available in the following publicly accessible repository https://www.star.nesdis.noaa.gov/socd/mecb/sar/AKDEMO_products/APL_winds/tropical/index.html. Sentinel data are obtained from https://scihub.copernicus.eu/dhus. *RADARSAT-2* data are provided by https://mda.space/en/. Data used to generate the results are available upon request.

## REFERENCES

Alpers, W., B. Zhang, A. Mouche, K. Zeng, and P. W. Chan, 2016: Rain footprints on C-band synthetic aperture radar images of the ocean—Revisited. *Remote Sens. Environ.*, **187**, 169–185, https://doi.org/10.1016/j.rse.2016.10.015.

Bliven, L. F., and J.-P. Giovanangeli, 1993: An experimental study of microwave scattering from rain- and wind-roughened seas. *Int. J. Remote Sens.*, **14**, 855–869, https://doi.org/10.1080/01431169308904382.

Boerner, W.-M., W.-L. Yan, A.-Q. Xi, and Y. Yamaguchi, 1992: Basic concepts of radar polarimetry. *Direct and Inverse Methods in Radar Polarimetry*, W.-M. Boerner et al., Eds., NATO ASI Series, Vol. 350, Springer, 155–245, https://doi.org/10.1007/978-94-010-9243-2_8.

Center for Satellite Applications and Research, 2020: SAROPS tropical storm winds demonstrator. NOAA, https://www.star.nesdis.noaa.gov/socd/mecb/sar/AKDEMO_products/APL_winds/tropical/index.html?year=2020.

Dunion, J., M. D. Eastin, D. S. Nolan, J. Hawkins, and C. Velden, 2010: Arc clouds in the tropical cyclone environment: Implications for TC intensity change. *29th Conf. on Hurricanes and Tropical Meteorology*, Tucson, AZ, Amer. Meteor. Soc., 6C.7, https://ams.confex.com/ams/29Hurricanes/techprogram/paper_168620.htm.

European Space Agency, 2020: Sentinel-1 SAR user guide. European Space Agency, https://sentinel.esa.int/web/sentinel/user-guides/sentinel-1-sar.

——, 2022: RADARSAT-1 & 2 full archive and tasking. European Space Agency, https://earth.esa.int/eogateway/catalog/radarsat-1-2-full-archive-and-tasking.

Foster, R. C., 2005: Why rolls are prevalent in the hurricane boundary layer. *J. Atmos. Sci.*, **62**, 2647–2661, https://doi.org/10.1175/JAS3475.1.

Friedman, K. S., and X. Li, 2000: Monitoring hurricanes over the ocean with wide swath SAR. *Johns Hopkins APL Tech. Dig.*, **21**, 80–85.

Fu, L., and B. Holt, 1982: SEASAT views oceans and sea ice with synthetic-aperture radar. NASA Tech. Rep. 82N24604, 206 pp., https://ntrs.nasa.gov/api/citations/19820016728/downloads/19820016728.pdf.

Hersbach, H., A. D. Stoffelen, and S. de Haan, 2007: An improved C-band scatterometer ocean geophysical model function: CMOD5. *J. Geophys. Res.*, **112**, C03006, https://doi.org/10.1029/2006JC003743.

Houze, R. A., Jr., S. S. Chen, B. F. Smull, W.-C. Lee, and M. M. Bell, 2007: Hurricane intensity and eyewall replacement. *Science*, **315**, 1235–1239, https://doi.org/10.1126/science.1135650.

Katsaros, K. B., P. W. Vachon, P. G. Black, P. P. Dodge, and E. W. Uhlhorn, 2000: Wind fields from SAR: Could they improve our understanding of storm dynamics? *Johns Hopkins APL Tech. Dig.*, **21**, 86–93.

Knaff, J. A., and J. F. Weaver, 2000: A mesoscale low-level thunderstorm outflow boundary associated with Hurricane Luis. *Mon. Wea. Rev.*, **128**, 3352–3355, https://doi.org/10.1175/1520-0493(2000)128<3352:AMLLTO>2.0.CO;2.

Li, X., W. G. Pichel, M. He, S. Y. Wu, K. S. Friedman, P. Clemente-Colon, and C. Zhao, 2002: Observation of hurricane-generated ocean swell refraction at the Gulf Stream north wall with the RADARSAT-1 synthetic aperture radar. *IEEE Trans. Geosci. Remote Sens.*, **40**, 2131–2142, https://doi.org/10.1109/TGRS.2002.802474.

——, J. A. Zhang, X. Yang, W. G. Pichel, M. Demaria, D. Long, and Z. Li, 2013: Tropical cyclone morphology from spaceborne synthetic aperture radar. *Bull. Amer. Meteor. Soc.*, **94**, 215–230, https://doi.org/10.1175/BAMS-D-11-00211.1.

Maxar Technologies, 2018: RADARSAT-2 product description. MDA Rep. RN-SP-52-1238, 91 pp., https://earth.esa.int/eogateway/documents/20142/0/Radarsat-2-Product-description.pdf/f2783c7b-6a22-cbe4-f4c1-6992f9926dca.

Melsheimer, C., W. Alpers, and M. Gade, 2001: Simultaneous observations of rain cells over the ocean by the synthetic aperture radar aboard the ERS satellites and by surface-based weather radars. *J. Geophys. Res.*, **106**, 4665–4677, https://doi.org/10.1029/2000JC000263.

Monaldo, F. M., and R. Beal, 2004: Wind speed and direction. SAR marine users manual, NOAA Doc., 305–320.

Montgomery, M. T., V. A. Vladimirov, and P. V. Denissenko, 2002: An experimental study on hurricane mesovortices. *J. Fluid Mech.*, **471**, 1–32, https://doi.org/10.1017/S0022112002001647.

——, M. M. Bell, S. D. Aberson, and M. L. Black, 2006: Hurricane Isabel (2003): New insights into the physics of intense storms. Part I: Mean vortex structure and maximum intensity estimates. *Bull. Amer. Meteor. Soc.*, **87**, 1335–1348, https://doi.org/10.1175/BAMS-87-10-1335.

National Aeronautics and Space Administration, 2020: Remote sensors. Earthdata, accessed, https://earthdata.nasa.gov/learn/remote-sensors.

Reppucci, A., S. Lehner, J. Schulz-Stellenfleth, and S. Brusch, 2010: Tropical cyclone intensity estimated from wide swath SAR images. *IEEE Trans. Geosci. Remote Sens.*, **48**, 1639–1649, https://doi.org/10.1109/TGRS.2009.2037143.

Sapp, J. W., S. O. Alsweiss, Z. Jelenak, P. S. Chang, S. J. Frasier, and J. Carswell, 2016: Airborne co-polarization and cross-polarization observations of the ocean-surface NRCS at C-band. *IEEE Trans. Geosci. Remote Sens.*, **54**, 5975–5992, https://doi.org/10.1109/TGRS.2016.2578048.

Shapiro, L. J., and H. E. Willoughby, 1982: The response of balanced hurricanes to local sources of heat and momentum. *J. Atmos. Sci.*, **39**, 378–394, https://doi.org/10.1175/1520-0469(1982)039<0378:TROBHT>2.0.CO;2.

Sitkowski, M., J. P. Kossin, and C. M. Rozoff, 2011: Intensity and structure changes during hurricane eyewall replacement cycles. *Mon. Wea. Rev.*, **139**, 3829–3847, https://doi.org/10.1175/MWR-D-11-00034.1.

Smith, R. K., 1980: Tropical cyclone eye dynamics. *J. Atmos. Sci.*, **37**, 1227–1232, https://doi.org/10.1175/1520-0469(1980)037<1227:TCED>2.0.CO;2.

Valenzuela, G. R., 1978: Theories for the interaction of electromagnetic and oceanic waves—A review. *Bound.-Layer Meteor.*, **13**, 61–85, https://doi.org/10.1007/BF00913863.

Vinour, L., S. Jullien, A. Mouche, C. Combot, and M. Mangeas, 2021: Observations of tropical cyclone inner-core fine-scale structure, and its link to intensity variations. *J. Atmos. Sci.*, **78**, 3651–3671, https://doi.org/10.1175/JAS-D-20-0245.1.

Willoughby, H. E., 1990: Temporal changes of the primary circulation in tropical cyclones. *J. Atmos. Sci.*, **47**, 242–264, https://doi.org/10.1175/1520-0469(1990)047<0242:TCOTPC>2.0.CO;2.

Zhang, B., and W. Perrie, 2014: Recent progress on high wind-speed retrieval from multipolarization SAR imagery: A review. *Int. J. Remote Sens.*, **35**, 4031–4045, https://doi.org/10.1080/01431161.2014.916451.

Zhang, G., and W. Perrie, 2018: Symmetric double-eye structure in Hurricane Bertha (2008) imaged by SAR. *Remote Sens.*, **10**, 1292, https://doi.org/10.3390/rs10081292.

Zhang, J. A., and X. Li, 2017: Tropical cyclone multiscale wind features from spaceborne synthetic aperture radar. *Hurricane Monitoring with Spaceborne Synthetic Aperture Radar*, X. Li, Ed., Springer Natural Hazards, Springer, 25–39, https://doi.org/10.1007/978-981-10-2893-9_2.

——, K. B. Katsaros, P. G. Black, S. Lehner, J. R. French, and W. M. Drennan, 2008: Effects of roll vortices on turbulent fluxes in the hurricane boundary layer. *Bound.-Layer Meteor.*, **128**, 173–189, https://doi.org/10.1007/s10546-008-9281-2.